Lab on a Chip

PAPER

View Article Online
View Journal

Cite this: DOI: 10.1039/d6lc00140h

Acoustofluidic separation of oblate spheroids from spheres using acoustic radiation torque and force

Muhammad Soban Khan,[a] Mushtaq Ali,[a] Yong Bin Bang,[b] Seong Jae Lee *[b] and Jinsoo Park *[a]

Cells, bacteria, and other bioparticles exist in diverse shapes, and their morphology plays a pivotal role in biological functions and clinical significance. Various microfluidic approaches have been developed for shape-based separation of bioparticles with the same or similar volume; however, most of them were limited to separation of prolate spheroids from spheres or required *a priori* labeling and consequent detection. Here, we propose a vertical-type acoustofluidic method for the first separation of oblate spheroids from spheres in a label-free manner. The acoustic radiation torque suppresses the rotational motion of oblate micro-objects, leading to horizontal alignment with an increase in projected surface area compared to that of isovolumetric spheres. The enhanced acoustic radiation force, proportional to the projected surface area normal to the wave propagation, allows the oblate spheroids to have greater vertical migration inside a microchannel, resulting in distinct trajectories for shape-based separation. We conduct numerical simulations of asymmetric wave scattering to elucidate the working principle and experiments to demonstrate the separation of polystyrene microparticles and red blood cells of spherical and oblate shapes at high purity and recovery rate. The proposed acoustofluidic approach holds promise for label-free, shape-based manipulation of bioparticles in cell biology and microbiology.

Received 12th February 2026,
Accepted 28th April 2026

DOI: 10.1039/d6lc00140h

rsc.li/loc

1. Introduction

Cells, bacteria, and other bioparticles exhibit diverse shapes that significantly influence their biological functions and clinical relevance.[1–4] Human cells exhibit a diverse range of shapes that are crucial for their functions: for instance, immune functions of macrophages,[5] epithelial-to-mesenchymal cancer cell progression,[6] and metastatic potential of tumor cells.[7] Specifically, human red blood cells (RBCs) exhibit a characteristic biconcave shape, with a diameter of 6–8 μm under healthy conditions, which enhances their flexibility and oxygen exchange efficiency.[8,9] Alterations in RBC morphology are closely associated with pathological conditions, often leading to changes in mechanical properties and reduced oxygen-carrying capacity.[10] For example, malaria-infected RBCs transform from their native biconcave shape into a more spherical form,[11] while hereditary spherocytosis also results in spherical RBCs due to membrane defects.[12] Elongated or elliptical RBCs are associated with elliptocytosis,[10] whereas sickle- or crescent-shaped RBCs are characteristic of sickle cell disease.[13] In addition, teardrop-shaped RBCs are indicative of myelofibrosis.[14] Therefore, the ability to identify and separate bioparticles based on shape is of significant importance for biomedical diagnostics, disease monitoring, and therapeutic assessment.[15,16]

Various microfluidic approaches have been proposed for shape-based bioparticle manipulation with advantages including precise, non-invasive processing, reduced reagent consumption, versatility, and easy integration.[17–19] A few successful demonstrations include inertial microfluidics for separation of spherical and rod-shaped *Euglena gracilis* microalgae,[20,21] deterministic lateral displacement for separation of biconcave RBCs and elongated *Trypanosoma cyclops* parasites,[22,23] and hydrodynamic filtration for separation of erythrocytes blood leukocytes.[24] These approaches primarily rely on flow-induced hydrodynamic effects and often require precise channel geometries or specific flow conditions for effective separation. In contrast, acoustofluidic techniques enable contactless and label-free manipulation of non-spherical particles based on acoustic radiation torque (ART) and acoustic radiation force (ARF), allowing dynamic control over particle orientation and trajectory. In standing bulk acoustic wave[25–27] and standing

[a] Department of Mechanical Engineering, Chonnam National University, 77 Yongbong-ro, Buk-gu, Gwangju 61186, Republic of Korea.
E-mail: jinsoopark@jnu.ac.kr
[b] Department of Polymer Engineering, The University of Suwon, 17 Wauan-gil, Bongdam-eup, Hwaseong, Gyeonggi 18323, Republic of Korea.
E-mail: sjlee@suwon.ac.kr

surface acoustic wave[28,29] ART has been shown to suppress rotational motion of prolate spheroids, leading to orientation-dependent focusing. Building on this, we previously demonstrated the separation of prolate spheroids from isovolumetric microspheres in a travelling surface acoustic wave (TSAW) field.[30] However, these approaches have been largely limited to prolate–sphere separation. In such cases, ART-induced alignment reduces the projected surface area, resulting in weaker ARF. In contrast, the present work focuses on oblate spheroids, where alignment increases the projected surface area, leading to enhanced ARF and distinct migration behavior. A comprehensive overview of these techniques can be found in our recent review.[19,31]

Here, we present a vertical-type acoustofluidic platform that enables, to the best of our knowledge, the first shape-based separation of oblate spheroids from isovolumetric spheres in a contactless and label-free manner, achieved through the combined effects of TSAW-induced ART and ARF. In the vertical-type configuration, the vertical wave propagation, whose magnitude is approximately 2.5 times greater than that of the horizontal counterpart, is primarily utilized for separation of spherical and oblate micro-objects with enhanced separation efficiency and improved operational robustness. The TSAW-induced ART causes horizontal alignment of the oblate spheroids with an increase in the projected surface area normal to the wave propagation. The enhanced ARF on the oblate spheroids in the vertical direction due to the increased projected area allows their trajectory to be vertically shifted from the trajectory of the microspheres, leading to shape-based separation. We performed numerical simulations of wave scattering from oblate spheroids with varying orientation and aspect ratio (AR) to elucidate that the TSAW-induced ART and ARF are attributed to the asymmetric wave scattering. We also experimentally proved that the acoustic streaming effect is negligible to the acoustofluidic shape-based separation in the proposed platform. Based on the findings, we report the first demonstration of the shape-based separation of oblate and spherical polystyrene (PS) microparticles and RBCs at high purity and recovery rate of ~100%. We expect that the proposed acoustofluidic shape-based separation method holds promise in various fields including cell biology and microbiology.

2. Results and discussion

2.1. Device configuration

The proposed vertical-type acoustofluidic device consists of a straight interdigital transducer (IDT) on a piezoelectric lithium niobate ($LiNbO_3$) substrate with a polydimethylsiloxane (PDMS) microchannel with four inlets and two outlets, as shown in Fig. 1a. Suspended particles or cells were introduced through inlet 1 at a flow rate of 50 μl h^{-1} and directed downward using a vertical sheath flow of 200 μl h^{-1} from inlet 2, guiding them closer to the IDT. The suspensions were then sandwiched between two additional horizontal sheath flows from inlets 3 and 4, each at a flow rate of 100 μl h^{-1}, to achieve horizontal alignment. Unless otherwise specified, these flow rates were maintained for all experiments, resulting in a throughput of approximately 30–40 cells per s under the present operating conditions. It should be noted that the primary objective of this study is to demonstrate shape-based separation driven by the combined effects of ART and ARF rather than to achieve high-throughput performance. The throughput can be further improved through optimization of flow conditions and device design parameters. TSAWs generated by the IDT underneath the microchannel refract into the fluid at the Rayleigh angle (~22° for $LiNbO_3$/water interface), forming leaky longitudinal waves (LWs) within the channel. These acoustic waves induce both ART and ARF, leading to shape-dependent particle behaviors. Specifically, the ART arising from asymmetric side scattering promotes horizontal alignment of oblate spheroids. The ARF originating from asymmetries in forward and backward scattering on the horizontally aligned oblate spheroids (red in Fig. 1b) is greater than that exerted on the spheres (green in Fig. 1b) and thus drives further vertical migration of the oblate particles and cells. For direct observation of the vertical migration, we developed three-dimensional downstream bifurcation, which converts the

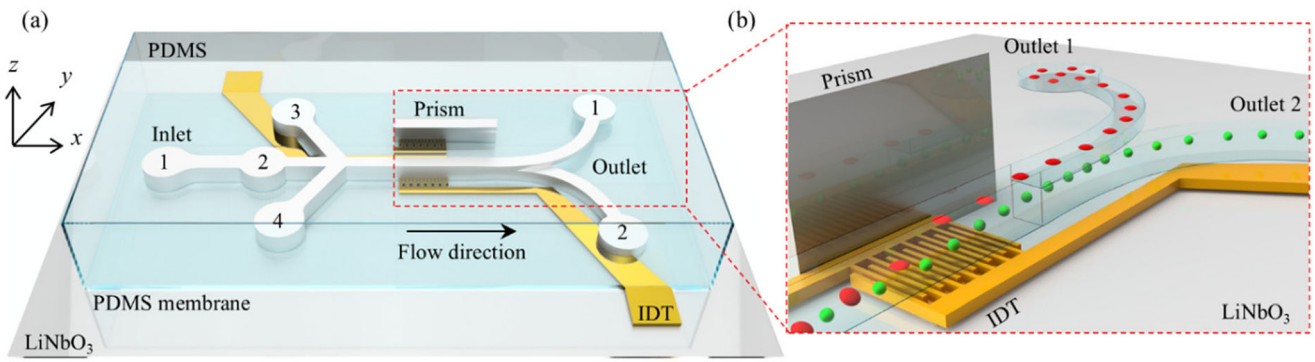

Fig. 1 (a) Schematic diagram of the vertical-type acoustofluidic device, (b) focused image showing a micro-prism for side-view visualization and a downstream vertical bifurcation diverging horizontally into two separate outlets.

two vertically distinguished particle trajectories into horizontal ones. However, because the vertical particle migration is inherently difficult to visualize directly through standard inverted or upright microscopy, we also embedded a prism mirror at the side of the microchannel.[32] This prism optically redirects the side view of the vertical particle trajectories into the microscope's imaging plane, allowing real-time visualization and direct confirmation of the vertical separation process during operation.

For electrical isolation of the fluidic region from the IDT electrodes while preserving acoustic coupling, a thin PDMS membrane is strategically placed between the microchannel and the substrate. This design eliminates direct contact between the fluid and the electrodes, minimizing particle and cell exposure to any residual fringing electric fields.[33] The PDMS insulating properties and dielectric behavior effectively suppress such fields, and the membrane structure provides additional practical advantages: it enables easy replacement of the microfluidic channel while reusing the same substrate, facilitating repeated experiments with consistent acoustic performance.[34,35] Although minimal residual electric fields may still penetrate, their influence is negligible compared to the acoustic effects, as investigated by Collins *et al.*,[36] who reported that the TSAW-induced ARF dominates over the accompanying electric forces by several orders of magnitude. This ensures that the observed particle behavior is primarily governed by the acoustic interactions.

2.2. Numerical investigation of asymmetric wave scattering from oblate spheroids with varying orientation and aspect ratio

Our hypothesis for the proposed shape-based separation of oblate spheroids from spheres in the proposed vertical-type acoustofluidic device is that (i) the rotational motion of the oblate spheroids is suppressed by the counter-rotating TSAW-induced ART, leading to horizontal alignment with their minor (shorter) axis (2b) parallel to vertical wave propagation (+z-direction) (Fig. 2a), and (ii) the increased projected area of the horizontally aligned oblate spheroids, perpendicular to the xy-plane in Fig. 1(a), results in an increase in the ARF magnitude, leading to further vertical migration compared to the spheres. For validation, we conducted numerical simulations for the wave scattering from oblate spheroids with varying AR as in Fig. 2. In the numerical calculation, we modeled a spherical PS particle with a diameter of 5 μm and its isovolumetric oblate particles with varying orientation and AR. Incident plane progressive waves are propagating in the +z-direction (from 270° to 90°) with a frequency of 141 MHz to have a κ value of 1.5 for effective PS particle manipulation by the ARF (ARF factor as a function of κ can be found in Fig. S1).[37] Fig. 2a demonstrates our numerical simulation model for acoustic wave scattering from oblate spheroids with varying orientation and AR, defined as the ratio of the minor axis (2b) divided by the major axis (2a). To isolate the primary vertical component of the leaky LWs, we modeled a +z-propagating plane wave and neglected lateral LW components (±x-direction) due to their minimal contribution to vertical migration. The oblate spheroid was placed within a computational domain of radius R_i, surrounded by a perfectly matched layer (PML) (for further details of numerical simulation, see the SI).

In our numerical approach, we simplified the phenomenon to focus on the dominant physical mechanisms, namely, the asymmetric wave scattering from oblate spheroids with varying orientation and AR. First, we modeled the fluid as inviscid, thereby neglecting the acoustic streaming effect induced by wave attenuation due to viscous damping. While acoustic streaming may be present, its influence on shape-based separation is minimal, as will be explained later with experimental validation (in section 2.7) because the particle size and wavelength under the operating conditions yield a Helmholtz number comparable to 1 (Mie scattering regime) where radiation dominates streaming effects.[38] Second, the assumption of rigid particles provides first-order approximation that captures the essential behavior of shape-induced responses without the added complexity

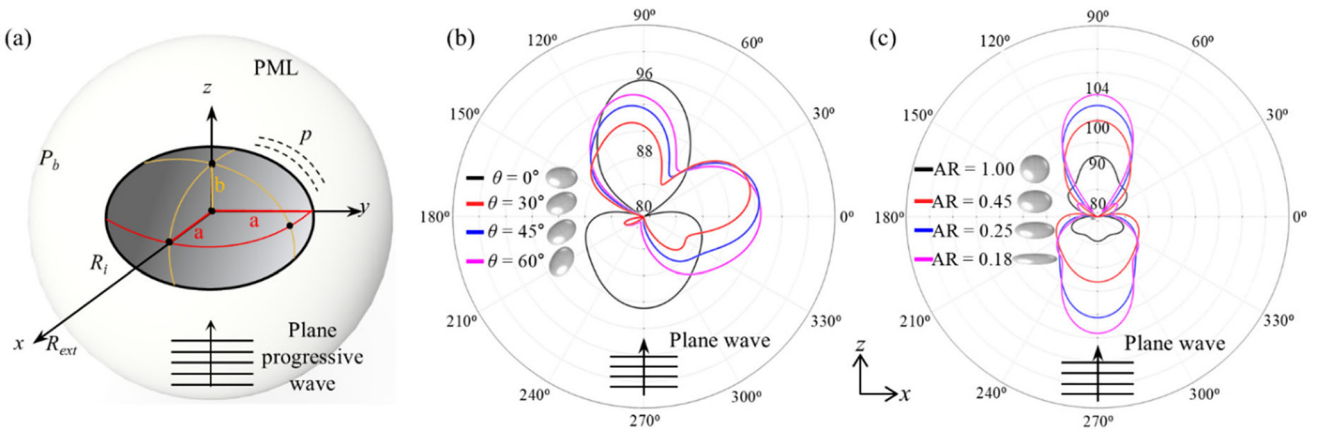

Fig. 2 (a) An oblate spheroid exposed to incident plane progressive waves. Polar scattering plots for oblate spheroids (b) with varying orientation (θ) of 0°, 30°, 45°, and 60° and (c) with varying aspect ratio (AR) of 1.00, 0.45, 0.25 and 0.18.

due to deformation. While biological particles like RBCs are indeed deformable, the dominant acoustic interactions, especially at moderate power levels, are primarily governed by geometry rather than minor morphological deformation. Third, the single-particle model neglects the particle-to-particle interaction effect such as secondary ARF. This is a reasonable approximation given the dilute sample conditions used in our experiments to minimize interparticle effects. However, we acknowledge that in high-concentration samples (*e.g.*, clinical RBC assays), these effects may become significant and should be addressed in future work. Overall, these assumptions are deliberate, enabling focused investigation of shape-specific ARF and ART without introducing insignificant confounding effects from viscous or collective dynamics.[39]

Fig. 2b shows a polar scattering plot for an oblate spheroid with an AR of 0.45 at varying orientations (θ) at a distance of R_{ext} = 100 μm. The wave scattering can be classified into forward (90°), backward (270°), and side scattering (0° and 180°).[30,40] The asymmetry in the side scattering generates an ART on the particle (ART formula available in the SI).[41–43] The oblate spheroids exhibit distinct rotational motions, including tumbling, kayaking, and log-rolling. These arise from the velocity gradient in a Poiseuille flow.[44] For θ = 0° (black), the two components of the side scattering were balanced, and no net torque was induced for the spheroid. On the other hand, for θ = 30° (red), 45° (blue), and 60° (magenta), asymmetric side scattering was observed, and the imbalance in the side scattering increased with increasing orientation. These results indicate that the TSAW-induced counter-rotating ART suppresses the rotational motion of the oblate spheroids. As a result, the particles align horizontally with the major axes (2a) aligned with the *xy*-plane to have θ = 0° in Fig. 2a. This alignment increases the projected surface area perpendicular to the wave propagation, resulting in the enhanced ARF, which is proportional to the projected surface area, exerted on the oblate objects.

A polar scattering plot for oblate spheroids with varying AR is shown in Fig. 2c. With reference to the sphere with AR = 1.00 (black), the isovolumetric oblate spheroids with AR = 0.45 (red), 0.25 (blue) and 0.18 (magenta) exhibited increasing backward scattering (270°) that is proportional to the ARF magnitude.[40] These results indicate that the magnitude of the ARF increases as the particle morphology changes from spherical (AR = 1) to oblate (smaller AR) and that the horizontally aligned oblate spheroids experience more significant ARF than the isovolumetric spheres. Further details on ARF and ART in terms of wave scattering can be found in the SI. As the oblate objects experience a larger magnitude of the ARF compared to the spherical objects with the same volume, we can infer that the oblate spheroids would show further vertical migration than the spheres in the proposed vertical-type acoustofluidic device. This difference in the vertical trajectories of two different shaped isovolumetric micro-objects allows separation at a downstream vertical bifurcation connected to separate outlets (Fig. 1b).

2.3. Fabrication of spherical and oblate PS microparticles

For experimental validation of the proposed acoustofluidic approach for the shape-based separation, we first fabricated PS microspheres and transformed them into oblate spheroids with varying AR by film-squeezing. The monodisperse PS spherical microparticles were synthesized by dispersion polymerization,[45,46] and the derivate oblate PS microparticles were fabricated by film-squeezing the spherical microparticles.[47] Further details can be found in the Experimental section. Fig. 3a–f present the SEM images of all the fabricated PS particles used in our experiments. The monodispersity of the PS microspheres with a diameter of 5 and 1.2 μm (Fig. 3a and e) was confirmed in the size distribution analysis in Fig. 3g. In the film squeezing process for the morphology transition from spherical to oblate, we varied the film squeezing pressure to fabricate oblate spheroids with varying AR of 0.45, 0.25, and 0.18 from the 5 μm PS spherical particles and with an AR of 0.18 from the 1.2 μm spherical particles, as shown in Fig. 3b–f, respectively. Although the oblate spheroids were found to be slightly polydisperse compared to the original microspheres, we found that the three kinds of the oblate spheroids had distinct size distributions (Fig. 3g).

2.4. Horizontal alignment of oblate spheroids by acoustic radiation torque

For experimental validation of the horizontal alignment of the oblate spheroids, we examined the orientation of spheres and oblate spheroids before and after the interaction with the TSAW field (Fig. 4 and Movie S1). The spheres might rotate in a Poiseuille flow, but their rotational motion cannot be observed due to the geometric symmetry in Fig. 4a and b. Both before and after interaction with the acoustic field, the spheres remained at the same focus. In contrast, the oblate spheroids displayed random orientations and rotational dynamics, mainly kayaking and tumbling, before encountering the acoustic field (Fig. 4c).[44] These freely rotating oblate particles experienced asymmetric side scattering when exposed to the traveling acoustic field; the rotational motion of the oblate spheroids was suppressed by the ART, resulting in horizontal alignment with their minor axis (2b in Fig. 2a) parallel to the vertical propagation of the leaky LWs (+*z*-direction), as shown in Fig. 4d. The inset images in Fig. 4d further confirm the horizontal alignment after the oblate spheroids passed through the acoustic field (see also Movie S1, corresponding to Fig. 4). The rotational dynamics of oblate particles in acoustic fields have been previously investigated. Hoque *et al.* reported that oblate particles experience acoustic radiation torque in standing wave fields, which governs their orientation and rotational behavior.[48] These findings are consistent with our observations, where ART suppresses rotational motion and

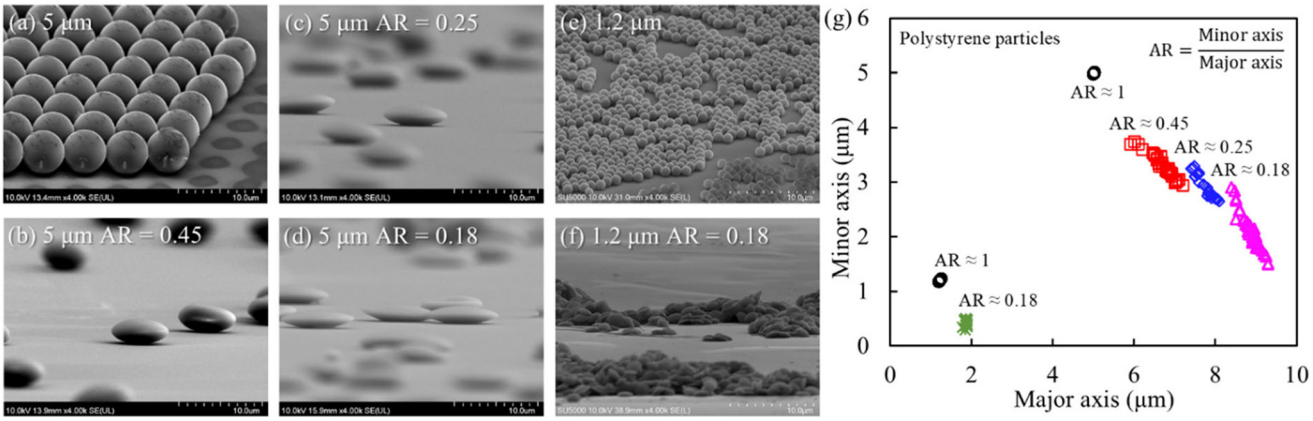

Fig. 3 SEM images of the 5 and 1.2 μm-diameter PS particles used in the experiments. (a and e) Original microspheres and oblate spheroids with AR of (b) 0.45, (c) 0.25, (d) 0.18, (f) 0.18 and (g) size distribution of the particles.

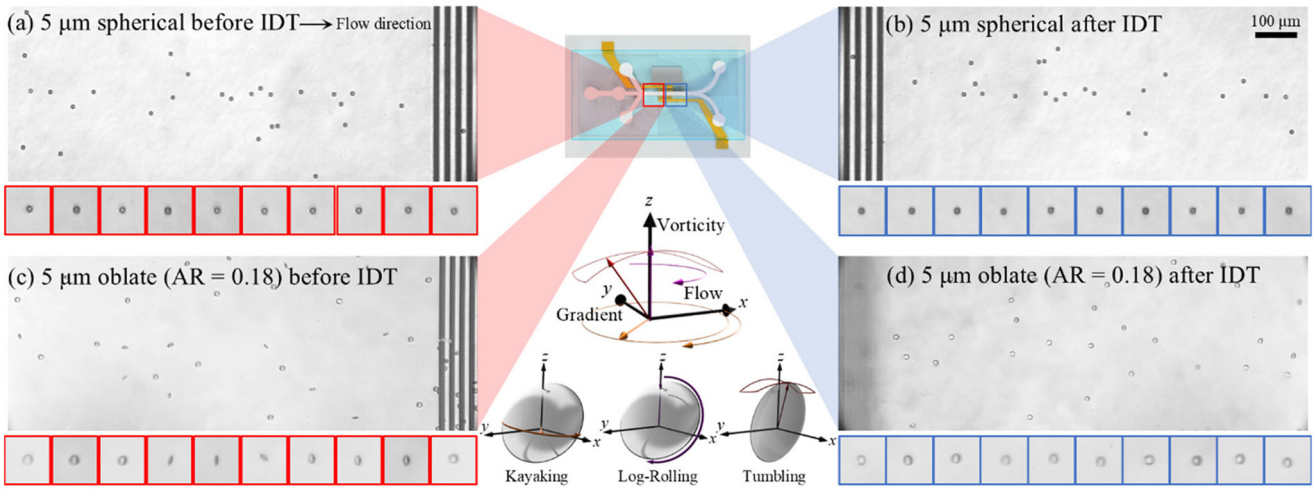

Fig. 4 Microscopic snapshot images of acoustofluidic vertical alignment of (a and b) spherical and (c and d) oblate microparticles.

induces stable horizontal alignment under TSAW excitation. The ART-induced horizontal alignment with major axes (2a in Fig. 2a) in the *xy*-plane increased the projected surface area normal to the wave propagation, thereby amplifying the net vertical ARF experienced by the oblate objects. As a result, unlike the spheres in Fig. 4a and b, the oblate spheroids exhibited a greater vertical migration distance; this increased vertical migration can be substantiated in Fig. 4d, where the oblate spheroids were captured at a higher focal plane approximately 600 μm above the IDT compared to their pre-alignment position in Fig. 4c. It should be noted that although both horizontal and vertical components of the acoustic wave are generated due to leakage at the Rayleigh angle (~22°), the vertical component becomes dominant in the present configuration. This is because the surface acoustic wave propagating along the substrate continuously leaks energy into the fluid at an oblique angle, resulting in a significant transfer of momentum in the vertical direction. Additionally, the confinement of the microchannel and the interaction of the leaky wave with the fluid–solid interface enhance upward acoustic radiation effects. As a result, the effective vertical component of the acoustic radiation force is significantly greater (approximately 2.5 times) than the horizontal component, making it the dominant factor governing particle trajectories in this vertical-type acoustofluidic platform.[49,50]

2.5. Investigation of vertical migration using a micro-prism: side-view visualization

The proposed acoustofluidic approach for the shape-based separation of oblate spheroids from spheres is based on varying vertical trajectory depending on the oblate spheroid AR. As the vertical migration of the particles is difficult to observe in conventional microcopy, we introduced a micro-prism alongside the microchannel for the side-view visualization of the particles, as shown in Fig. 5a. With the side illumination, the scattered fluorescence light can be detected in the microscopy through the mirror side of the prism.[32] As investigated earlier, the oblate

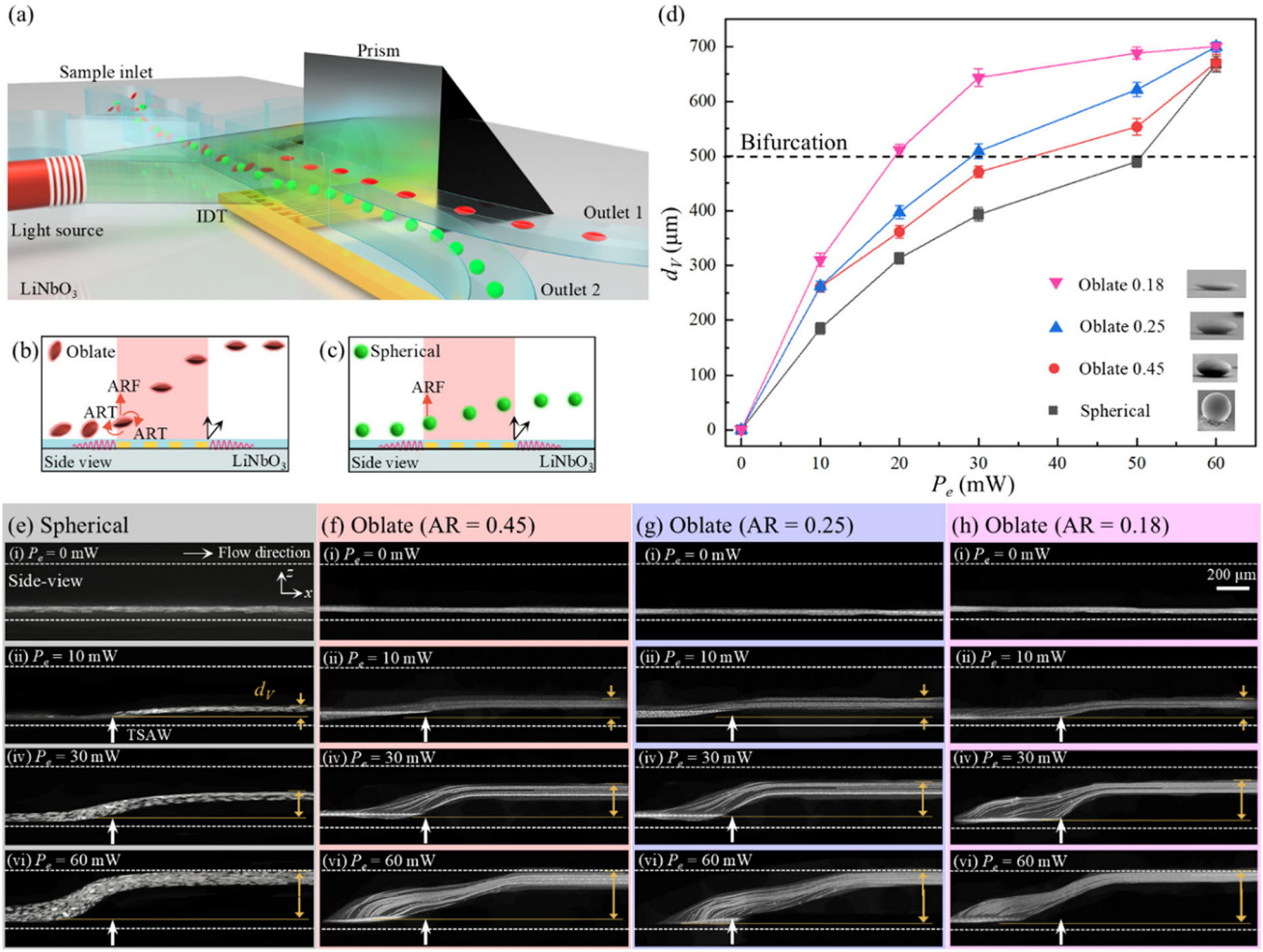

Fig. 5 (a) A schematic diagram of the proposed acoustofluidic device with a micro-prism for side-view visualization. Side view at midstream microchannel for (b) oblate and (c) spherical particles. (d) Vertical displacement (d_v) of the particles with varying AR and electrical power (P_e) applied to the IDT. (e–h) Microscopic prism view of the different particles.

particles are horizontally aligned by the ART and migrate vertically by the ARF (Fig. 5b) while the spherical particles experience only the ARF with its magnitude less than that exerted on the oblate ones (Fig. 5c) in the acoustic field. Fig. 5d summarizes the experimental results of the vertical displacement (d_V) as a function of the electrical power (P_e) applied to the IDT for spherical (black) and oblate particles with AR = 0.45 (red), 0.25 (blue), and 0.18 (magenta). Overall, with increasing P_e, the d_V value was measured to increase accordingly due to the increasing ARF magnitude proportional to P_e for all kinds of particles. As the particle shape changed from spherical to more oblate (smaller AR), the d_V value increased at the fixed P_e conditions because the ARF magnitude was enhanced by the increased projected area due to the horizontal alignment of the oblate particles caused by the ART.

Fig. 5e–h present the microscopic side-view images obtained through the prism, showing varying vertical migration of the particles depending on P_e and AR of the PS microparticles. The microchannel had a height of 700 μm with a downstream vertical bifurcation located 500 μm above the microchannel bottom. We confirmed that the side-view visualization of the fluorescent PS microparticles with varying AR can be achieved in our micro-prism-embedded microchannel. From the experimental results, by applying a frequency of 141 MHz, we found that the lower P_e required for the particles to reach the same d_V tended to decrease with decreasing AR (more oblate). In other words, at the same P_e, the d_V increased with decreasing AR. For example, at P_e = 30 mW, the d_V value was measured to be approximately 645, 510, 470, and 390 μm for AR = 0.18 (magenta), 0.25 (blue), 0.45 (red), and 1.00 (black), respectively. With the vertical bifurcation located 500 μm above the microchannel bottom, the oblate particles with AR = 0.18 and 0.25 with d_V greater than 500 μm can be collected in the upper outlet (outlet 1), while the spherical and oblate particles with AR = 0.45 with d_V smaller than 500 μm can be collected in the lower outlet (outlet 2), as will be demonstrated later.

Importantly, it should be noted that what enables the proposed shape-based separation is not the absolute value of

the vertical migration distance (d_V) but the relative migration difference (Δd_V) between the particle types. In our previous cross-type acoustofluidic platform,[30] we observed that the ART suppressed the rotation of prolate spheroids, thereby minimizing their projected area perpendicular to the wave propagation and reducing the ARF magnitude in comparison to the isovolumetric spheres. This enabled label-free separation between spherical and prolate particles, although the difference in lateral migration was limited to approximately 50 μm. In contrast, the proposed vertical configuration aligns the oblate spheroids such that their major axes align perpendicular to the vertical wave propagation, enhancing the interaction mainly with the vertical component of the travelling wave field, which is 2.5 times more significant that the horizontal counterpart due to the Rayleigh angle of 22° at the $LiNbO_3$/water interface. As a consequence, we achieved a vertical migration difference exceeding 100 μm, significantly enhancing separation efficiency and stability (Fig. 5). This enhanced migration not only improves the purity and robustness of particle separation but also offers valuable design insights. In the cross-type acoustofluidic platform, the projected surface area, normal to the horizontal ARF component, remains relatively unchanged between the oblate spheroids and the spheres; therefore, these two shapes cannot be effectively distinguished or separated. However, transitioning from the cross-type to vertical-type configurations addresses this limitation of the previous device, enabling the effective separation of oblate spheroids from spheres, which has remained as an unmet need despite importance and necessity.

2.6. Investigation of particle trajectories in a vertical bifurcation microchannel: bottom-view visualization

Fig. 6a–c illustrate the various particle trajectories depending on the particle shape at the downstream vertical bifurcation, connected to upper and lower outlets (outlets 1 and 2, respectively) for separate collection. In Fig. 5, the vertical displacement by the ARF was measured to be $d_V \cong 190$, 260, 260, and 310 μm at P_e = 10 mW, 395, 470, 510, and 643 μm at P_e = 30 mW, 660, 665, 690, and 700 μm at P_e = 60 mW for the spherical and oblate particles with AR = 1.00 (black), 0.45 (red), 0.25 (blue), and 0.18 (magenta), respectively. The downstream vertical bifurcation was installed at a height of 500 μm inside the microchannel and diverged horizontally into two separate outlets to allow bottom-view visualization under an inverted microscope. After the bifurcation, the vertical upper channel was connected to the horizontal upper outlet (outlet 1) while the vertical lower channel was linked to the horizontal lower outlet (outlet 2). In the bottom-view visualization (without micro-prism), a varying horizontal trajectory after the vertical bifurcation toward either outlet is observed in Fig. 6d, f, h, and j depending on the particle AR and wave amplitude (P_e applied to the IDT). Without the acoustic field, all the particles were flowing toward the lower outlet after the vertical bifurcation. The collected particle fractions from the two outlets as a function of P_e are shown in Fig. 6e, g, i, and k (black for upper outlet 1 and red for lower outlet 2); Fig. S2 presents fluorescence microscopy images of the green-fluorescence spherical and red-fluorescence oblate PS microparticles collected at outlet 1 and outlet 2. At P_e = 10 mW, the vertical

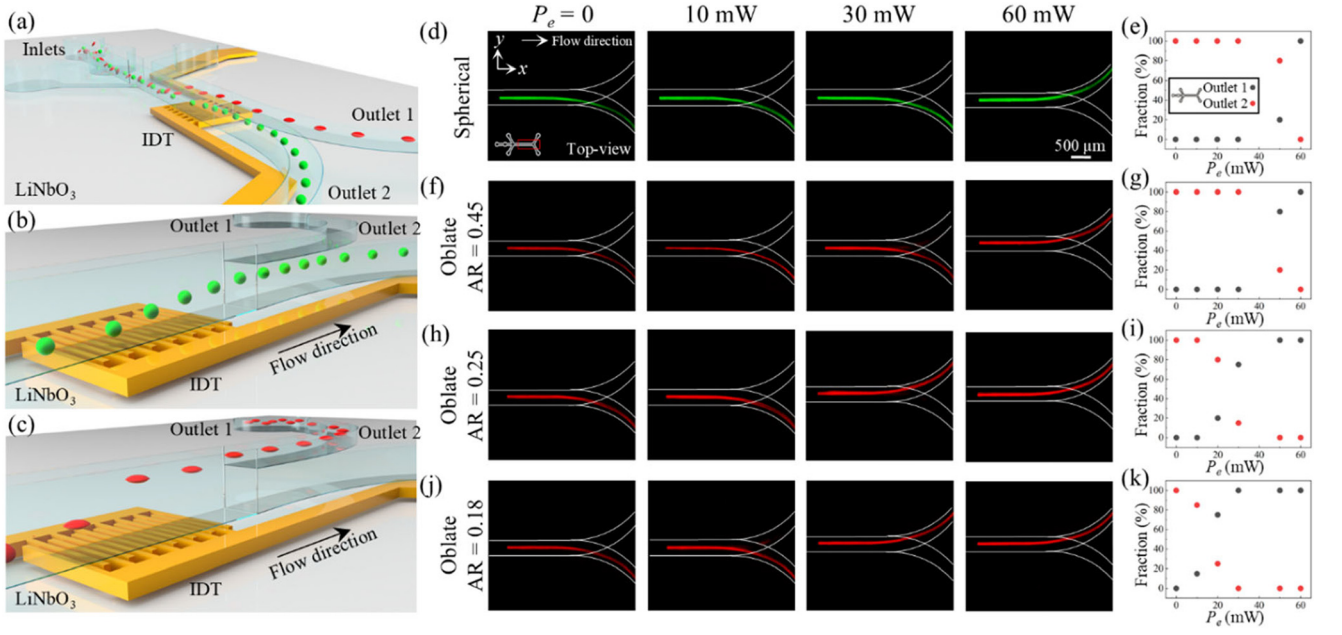

Fig. 6 (a–c) Illustrations of the trajectories of spherical and oblate particles in a vertical bifurcation microchannel. (d, f, h, and j) Bottom-view visualization of the spherical and oblate PS microparticles with different AR and P_e at the bifurcation. (e, g, i, and k) Particle distribution across the two outlets as a function of P_e.

migration for all the particles was smaller than the vertical bifurcation height, and all the particles were flowing through the lower outlet. On the other hand, at P_e = 30 mW, both oblate spheroids with AR = 0.25 and 0.18 showed the vertical migration greater than the vertical bifurcation and thus passed through the upper outlet (outlet 1) unlike the spherical and oblate particles with AR 0.45. With further increased P_e of 60 mW, all the particles experienced ARF with a sufficient magnitude to reach the microchannel ceiling and consequently migrated toward the upper outlet. These results suggest that the proposed acoustofluidic platform can be applicable to the shape-based separation of oblate spheroids from spheres depending on the particle shape under the same acoustic field at a fixed P_e condition.

2.7. Acoustofluidic shape-based separation of oblate spheroids from spheres

In the proposed acoustofluidic device with a vertical configuration, we hypothesized that the acoustic streaming effect was negligible to the demonstrated shape-based separation even in a relatively high channel (height of 700 μm) under high-frequency excitation at 141 MHz. This is attributed to our earlier claims that (i) it is not the vertical migration itself but the difference in the vertical migration that enables the proposed shape-based separation in the vertical-type acoustofluidic platform and that (ii) the frequency for separation was carefully chosen such that the scatter size (particles or cells) was comparable to the acoustic wavelength to induce the asymmetric Mie scattering for the ART and ARF acting on the scatter. For validation of our hypothesis, we conducted a negative-control experiment using the isovolumetric spherical (~1.2 μm) and oblate (AR of 0.25) particles (green and red fluorescence in Fig. 7, respectively) with low Helmholtz number. In this Rayleigh scattering regime, as the influence of the acoustic streaming dominated over the acoustic radiation, we could assume that the effects of the TSAW-induced ART and ARF were negligible. In other words, the vertical migration of the particles was solely attributed to the streaming-induced hydrodynamic force. As shown in Fig. 7, we found that both particles were flowing through the lower outlet regardless of the application of the acoustic field. It indicates that the shape-based separation cannot be achieved by the acoustic streaming effect. The acoustic streaming-induced hydrodynamic drag force might cause the vertical migration to some extent; however, it was equal for the particles of both shapes with no noticeable difference in the trajectories even under elevated P_e conditions up to 1.6 W (Fig. 7b), far exceeding the operational level (30 mW) for the radiation-based sorting (Fig. 6). From the observations, we can conclude that the main working principle of the proposed shape-based method is the combined effects of acoustic radiation and torque, not streaming.

Building on the numerical and experimental findings, we successfully demonstrated the shape-based separation of the oblate spheroids from the spherical particles in the proposed device in Fig. 8. For clear distinction in the fluorescence images and quantitative analysis of the separation efficiency, we used the red- and green-fluorescence PS microparticles with varying AR; however, this fluorescence labeling is simply for better visualization, not a prerequisite of the proposed label-free acoustofluidic shape-based separation. Fig. 8a demonstrates the acoustofluidic shape-based separation of the red-fluorescence oblate (AR = 0.18) and green-fluorescence spherical PS microparticles at P_e = 30 mW. The red oblate particles were horizontally aligned by the ART in the acoustic field and experienced greater ARF than the green spherical particles. All the red oblate particles were collected at upper outlet 1, while all the green spherical particles were

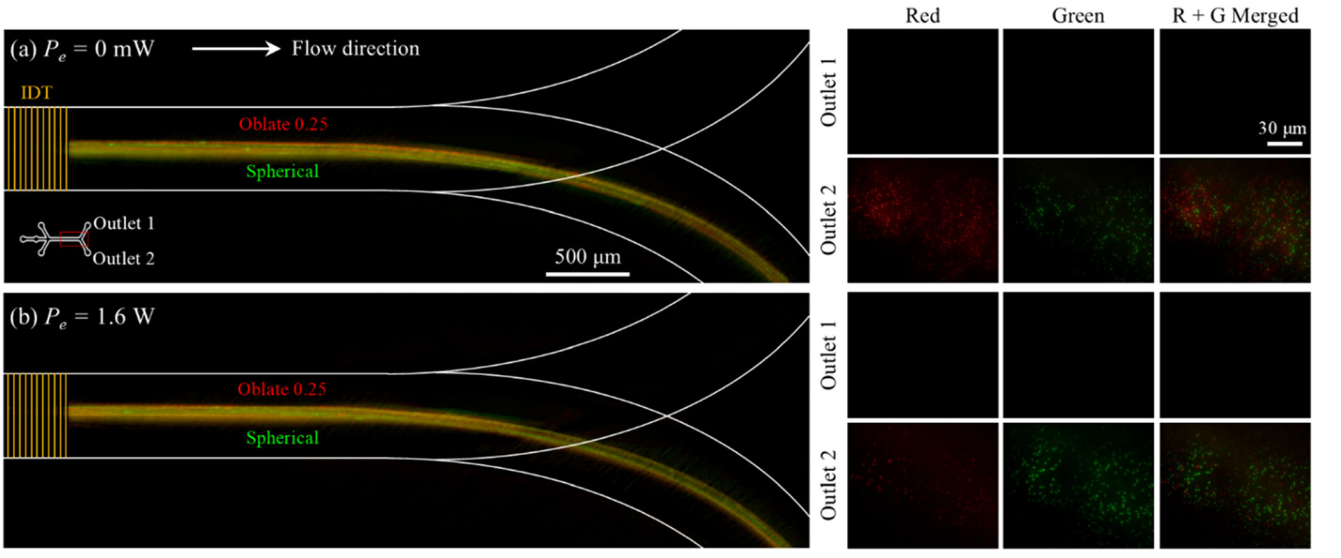

Fig. 7 Acoustofluidic shape-based separation of low Helmholtz number particles (~1 μm) of oblate and spherical shapes (a) without P_e and (b) with P_e.

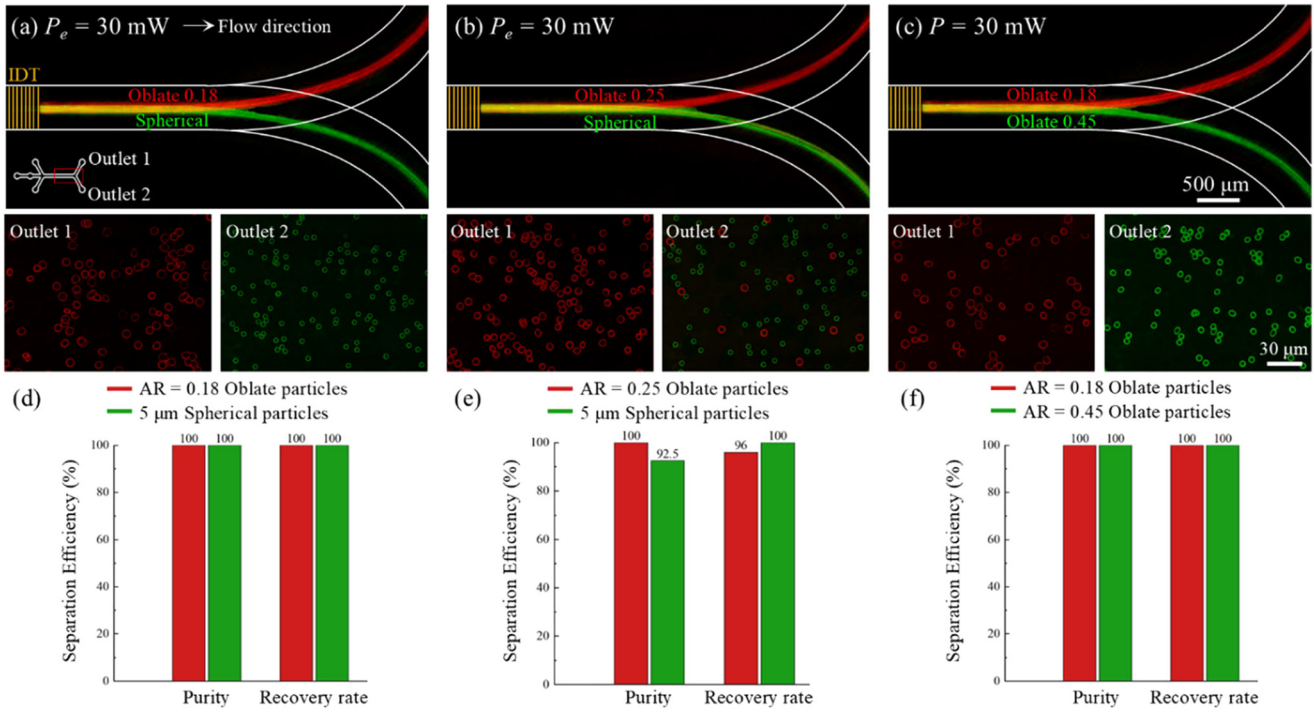

Fig. 8 Acoustofluidic shape-based separation of (a) oblate with AR = 0.18 and spherical, (b) oblate with AR = 0.25 and spherical, and (c) oblate with AR = 0.18 and 0.45. (d–f) Purity and recovery rate analysis for the collected particles after separation.

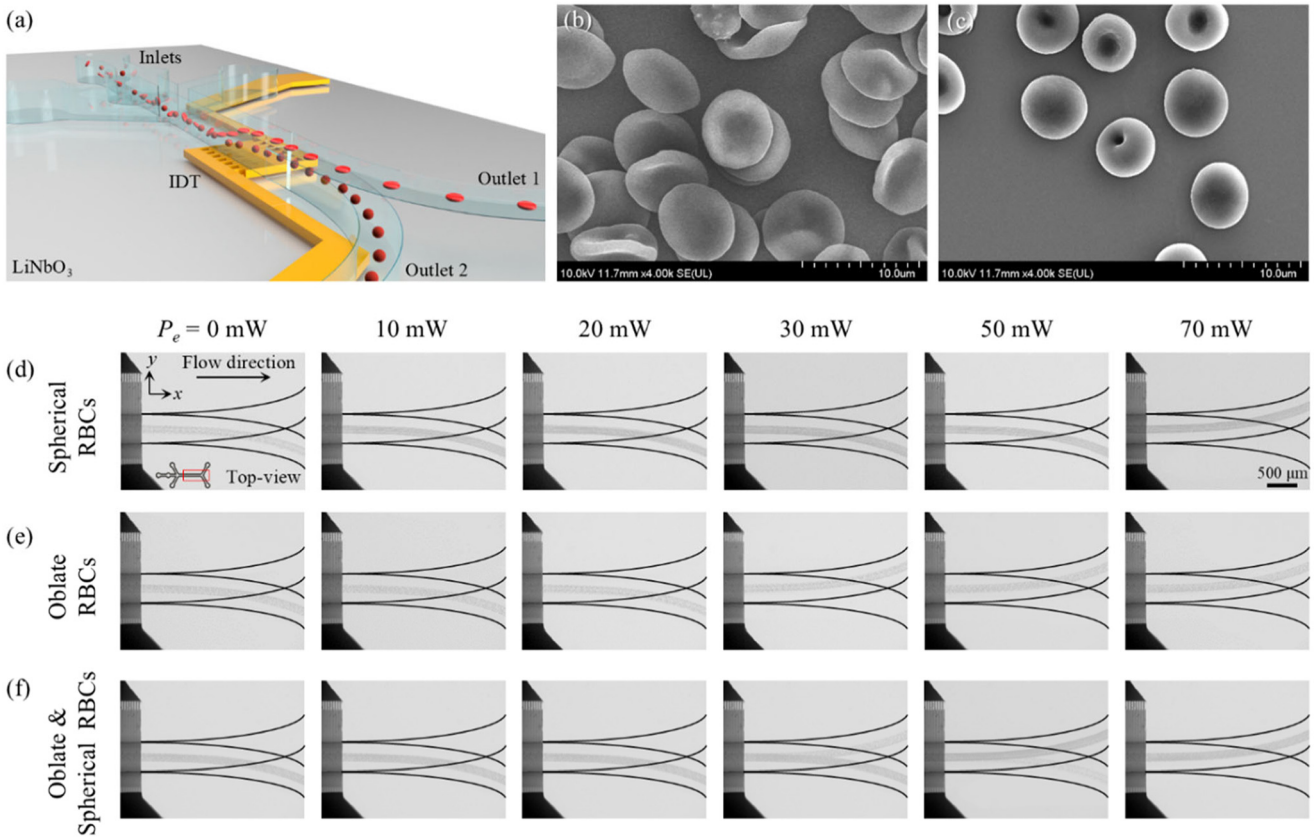

Fig. 9 (a) Schematic of vertical-type acoustofluidic device for the shape-based RBC sorting. Scanning electron micrographs of (b) normal biconcave-shaped RBCs prior to osmotic treatment and (c) RBCs in hypotonic solution (189 mOsm kg^{-1} H_2O). RBC sorting images for (d) spherical-shaped, (e) oblate-shaped, and (f) mixed RBCs at varying P_e.

retrieved at lower outlet 2 with 100% purity and recovery rate (Fig. 8d). In Fig. 8b, even with smaller AR difference, the similar results were obtained for the two distinct-shaped particles (red oblate with AR = 0.25 and green spherical) at P_e = 30 mW. A reduction in the AR difference led to a slight decrease in the purity of 100% and 92.5% and recovery rate of 96% and 100% for oblate (AR = 0.25) and spherical particles, respectively (Fig. 8e). The proposed acoustofluidic shape-based separation method was found to be applicable to not only between the spherical and the oblate particles, but also between the oblate spheroids with different ARs. Fig. 8c shows that the red-fluorescence oblate particles with AR = 0.18 can be separated from the green-fluorescence oblate particles with AR = 0.45 at P_e = 30 mW. Both oblate spheroids were horizontally aligned by the ART in the acoustic field. As in our numerical simulation results in Fig. 2c, the more oblate-shaped spheroids (red, AR = 0.18) experienced the greater magnitude of the ARF than the less oblate-shaped spheroids (green, AR = 0.45) due to the greater acoustic backward scattering caused by the larger projected surface area. All the red oblate particles with AR = 0.18 were collected at the upper outlet 1, while all the green oblate particles with AR = 0.48 were retrieved at the lower outlet 2 with 100% purity and recovery rate (Fig. 8f). All the results in Fig. 8 were in good agreement in the sorting experiments in Fig. 5 and 6.

2.8. Acoustofluidic shape-based separation of oblate and spherical RBCs

For validation of the practical applicability, we applied the proposed acoustofluidic approach for the separation of oblate and spherical RBCs, as shown in Fig. 9. We modified the normal oblate RBC morphology into the sphere based on osmolarity-dependent shape transition. We used a NaCl solution of 189 mOsm kg^{-1} H_2O to achieve the spherical-shaped RBCs without compromising their integrity.[51] We first conducted the RBC sorting experiments separately for the spherical and oblate RBCs, in which the latter samples required the osmolarity-induced RBC shape change. Fig. 9a illustrates the acoustofluidic shape-based RBC separation in the proposed device. The SEM images confirmed the biconcave RBC shape without any treatment (Fig. 9b) and the osmolarity-induced spherical-like RBCs (Fig. 9c), in which the RBC volume remained almost the same. We conducted the RBC sorting experiments with a frequency of 65 MHz tailored to the RBC properties (details can be found in Fig. S2). Fig. 9d shows the varying trajectory of the morphology-altered spherical RBCs at the vertical bifurcation depending on P_e applied to the IDT. Due to the spherical shape, the abnormal RBCs experienced comparably less ARF and thus flowed toward the lower outlet until P_e = 50 mW. With the increased P_e of 70 mW, the spherical RBCs vertically migrated farther than 500 μm and thus were collected at the upper outlet 1. On the other hand, the biconcave normal RBCs in Fig. 9e experienced the TSAW-induced ART due to the asymmetric side scattering, leading to the horizontal RBC alignment. The increased projected surface area caused the ARF acting on them to increase so that their vertical migration was greater than that of the spherical RBCs under the same acoustic intensity conditions. The vertical trajectory transition of the normal RBCs was observed at P_e = 30 mW, lower than the threshold power required for the spherical RBCs (P_e = 70 mW in Fig. 9d).

Following the sorting experiments, we conducted simultaneous separation experiments using mixed populations of spherical and oblate, disc-shaped RBCs, as shown in Fig. 9f. Until a low P_e of up to 20 mW was applied to the transducer, neither spherical nor oblate RBCs experienced sufficient ARF to have a vertical migration exceeding 500 μm (location of the vertical bifurcation at downstream). Both spherical and oblate RBCs were collected from the lower outlet (outlet 2), as can be expected from the independent sorting experiment results. Upon increasing the power up to 30 mW, significant ARF was exerted on the horizontally oriented oblate RBCs, leading to their trajectories being translocated to the upper outlet (outlet 1), separated from the spherical RBCs. At P_e = 50 mW, even a few non-target spherical RBCs exhibited sufficient vertical migration and passed through the upper outlet, together with the oblate RBCs. At P_e = 70 mW, both oblate and spherical RBCs experienced significant ARF and thus vertically migrated into the upper outlet 1.

For quantitative evaluation of the shape-based RBC separation efficiency, we utilized the fluorescence-labeled RBCs (oblate in green and spherical in red) even though the proposed acoustofluidic approach does not require any label for separation. The labeling did not affect cell morphology or behavior but enabled fluorescence-based analysis of the RBCs with two different shapes. Fig. 10 shows the purity of the collected abnormal spherical and normal oblate RBCs at both outlets at varying P_e applied to the transducer. For quantification, we calculated the purity by assuming the oblate and spherical RBCs as the targets for the upper and lower outlets, respectively. From P_e of 0 to 20 mW, the purity of the abnormal RBCs was 50% as both oblate and spherical RBCs were all collected in the lower outlet (Fig. 10a–c). At P_e = 30 mW, the purity of the normal RBCs with green fluorescence at outlet 1 was 100%, while that of the abnormal RBCs with red fluorescence at outlet 2 was 86%, indicating a few oblate RBCs remained with the spherical RBCs (Fig. 10d). This impurity may be attributed to the non-uniformity of the normal RBCs in size and shape, as shown in Fig. 9b. With the elevated power of 50 mW, on the other hand, the purity of the abnormal, spherical RBCs increased to 100%, while that of the normal, oblate RBCs reduced to 90%, since a few spherical RBCs vertically migrated to the upper outlet (Fig. 10e) due to the polydispersity in shape and size, as shown in Fig. 9c. At P_e = 70 mW, the purity of the normal RBCs was 50% as all the RBCs were collected in the upper outlet (Fig. 10f). These results underscore the importance of

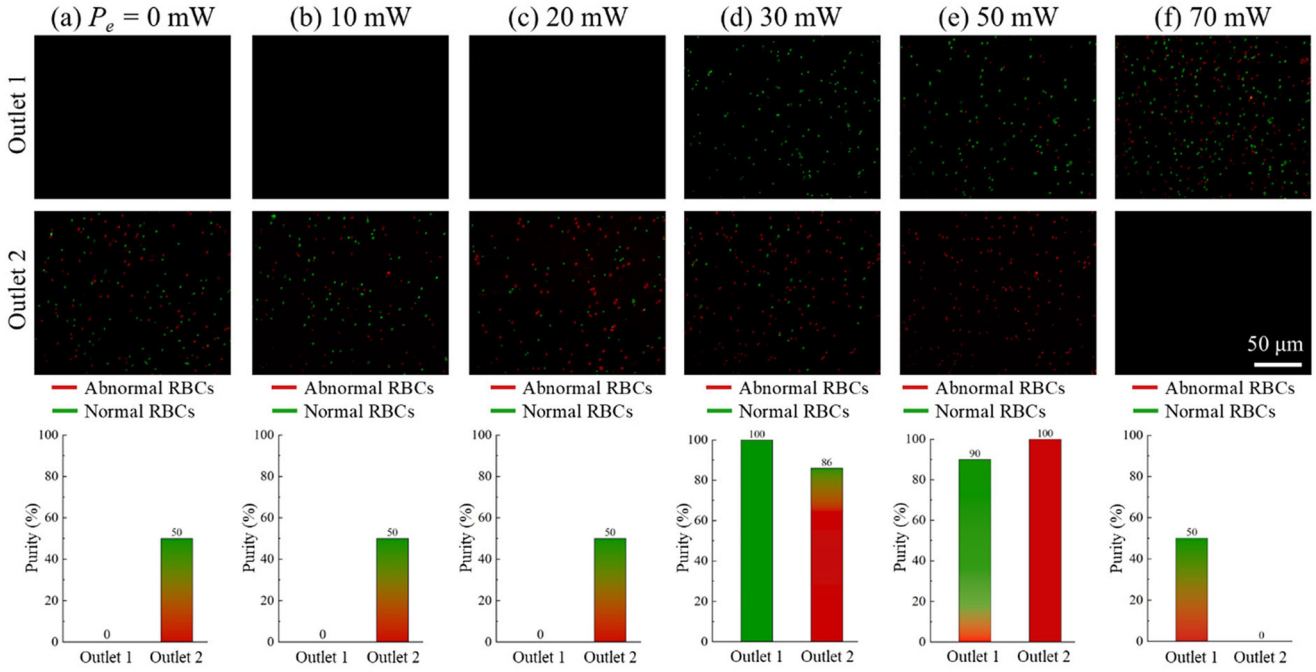

Fig. 10 (a–f) Quantitative evaluation of the shape-based RBC separation by the collected samples at the outlets at different P_e with their purity at each outlet.

the optimization of the operating conditions, especially P_e, for efficient acoustofluidic shape-based separation. It should be highlighted that the proposed acoustofluidic device in the vertical configuration enables the first demonstration of RBC separation based on the cell morphology in a label-free manner.

It is worth noting that the magnitude of the ARF exerted on an object is proportional to the wave amplitude squared and also the electrical power applied to the transducer,[52] regardless of acoustic frequency. In our experiments, we used the 5 μm spherical PS particles and their derivative isovolumetric oblate particles with varying aspect ratio, whereas the normal oblate RBC size ranged from 6 to 8 μm under healthy conditions. The non-uniform size distribution of the oblate particles (Fig. 3g) and RBCs (Fig. 9b and c) might have reduced the separation efficiency in the experimental demonstrations. Moreover, in Fig. 8, the separation of isovolumetric oblate and spherical PS particles was achieved at P_e of 30 mW. In contrast, in Fig. 10, we applied a comparable or larger P_e for separation of the oblate and spherical RBCs, although the RBC size was larger than that of the PS particles. This can be attributed to the reduced difference in acoustic impedance contrast for the RBCs compared to the PS microparticles. As the acoustic impedance contrast at the RBC/water interface was smaller than that at the PS particle/water interface, the higher electrical power would have been applied for the shape-based RBC separation.

It is important to note that healthy RBCs typically exhibit a relatively uniform biconcave (discocyte) morphology with limited variation in aspect ratio under physiological conditions. In contrast, under pathological conditions such as hereditary spherocytosis, RBCs transform from biconcave discocytes into near-spherical spherocytes due to membrane loss and structural alterations, resulting in a significant reduction in shape anisotropy.[53] In this study, spherical particles are used as representative models for such abnormal RBC morphologies. Therefore, the proposed method is particularly suited for separating particles with pronounced shape differences, while separation of subtle variations within healthy RBC populations is beyond the scope of the present work.

3. Conclusions

We developed an acoustofluidic platform in the vertical configuration for shape-based separation of oblate spheroids from spheres in a label-free manner based on the TASW-induced ART and ARF. Our numerical and experimental investigations revealed that asymmetric side scattering exerts a counterrotating ART on the oblate particles, repressing the rotation of the oblate objects and thus aligning their shorter, minor axis parallel to the wave propagation. This horizontal alignment increases the projected surface area of the oblate spheroids to the vertical wave propagation, enhancing backward scattering and amplifying the ARF. The increased ARF acting on the oblate micro-objects allows them to have further vertical migration than the isovolumetric spherical ones. Based on these findings, we successfully demonstrated the shape-based separation of spherical and oblate PS microparticles and RBCs at high purity and recovery rate.

4. Experimental

Microfluidic device

The IDT was composed of a bimetallic layer of Cr and Au (thickness of 20 and 100 nm, respectively) deposited on a 500 μm-thick 128°-rotated, Y-cut, X-propagating $LiNbO_3$ substrate (MTI Korea) by means of photolithography, E-beam evaporation, and lift-off procedure.[54] Two sets of IDTs were utilized in the experiments, one having a comb-shaped electrode spacing ($\lambda/4$) of 7 μm and the other with a comb-shaped electrode spacing ($\lambda/4$) of 15.2 μm with a total aperture of 1 mm and consists of 30 electrode pairs. A vector network analyzer (E5071B, Agilent Technologies) was used to determine the resonant frequency of the straight IDTs as 141 MHz and 65 MHz, respectively. Fig. S3 shows the S_{11} measurement data of both IDTs by a vector network analyzer. For applications of RF AC signals to the straight IDT, an RF signal generator (BSG F10, Belektronig GmbH) was used. To fabricate the bifurcated rectangular PDMS microchannel, a 3D mold was created using a 3D printer and then the soft lithography process was performed to create a 3D microchannel. The mold was pretreated with 1*H*,1*H*,2*H*,2*H*-perfluorooctyltriethoxysilane (Sigma-Aldrich) before pouring the PDMS mixture (Sylgard 184A and 184B, Dow Corning) on it. The rectangular microchannel had a height (h) of 700 μm and a width (w) of 300 μm. A micro-prism of 2 mm × 2 mm (N-BK7 Right Angle Prism, Edmund Optics Worldwide) was placed on the side of the microchannel 2 mm away from the microchannel wall. After fabricating the prism-embedded microchannel, the microchannel chip was bonded to the substrate using oxygen plasma treatment (Covance, Femto Science). Fluorescent PS microspheres with a diameter of 5 μm were sourced from Thermo Scientific, Inc. The sample and sheath fluid were injected into the microchannel using a syringe pump (neMESYS Cetoni GmbH) with particles suspended in distilled water (Dyne Bio Inc). To observe the behavior of the particles, we used a high-speed CMOS camera (VEO 710 L, Phantom) paired with an inverted microscope (IX73, Olympus).

Microparticle fabrication

To fabricate PS spherical microparticles with a diameter of 5 μm, 1.6 g of polyvinylpyrrolidone (PVP, Sigma-Aldrich) was first dissolved in 210 g of butanol and magnetically stirred for 1 h. The butanol solution containing PVP was added to a 40 g solution of styrene monomer containing 0.4 g of azobisisobutyronitrile (AIBN) in a 500 ml three-necked double-jacket reactor equipped with a reflux condenser, and then polymerization was initiated. The polymerization was performed at 70 °C and 120 rpm for 24 h under a N_2 atmosphere. For generation of oblate microparticles, polyvinyl alcohol (PVA) (Sigma-Aldrich) was used to prepare a polymer film containing monodisperse PS spherical microparticles for uniaxial squeezing. First, 7.5 g of PVA was added to 150 ml of distilled water at 80 °C and sufficiently dissolved using magnetic stirring for 4–5 h. 0.1 wt% PS spherical microparticles were added to this PVA aqueous solution. The uniformly dispersed mixture was poured onto a flat aluminum tray and dried to obtain a flexible PVA film containing PS spherical microparticles. For fabrication of oblate microparticles, the film was cut into a circular shape and placed between two silicone rubber sheets (HSW Co., South Korea) to form a three-layered composite. The composite consisting of these three layers was uniaxially squeezed using a press at 135 °C with a compression range of 17–83%. The squeezed film with different degrees of compression was dissolved in distilled water at 80 °C and then centrifuged to recover the PS oblate microparticles with different aspect ratios.

RBC fixation protocols

The following procedure outlines the cell fixation protocols for solutions used with RBCs in our succeeding experiments. We prepared a 2.5% glutaraldehyde solution by mixing 1 ml of 25% glutaraldehyde with 9 ml of phosphate-buffered saline (PBS), yielding a total volume of 10 ml. Similarly, we prepared 10 ml of 2% paraformaldehyde solution by combining 5 ml of 4% paraformaldehyde with 5 ml of PBS. The cells were fixed using the 2.5% glutaraldehyde solution with 5 ml of 2% paraformaldehyde for 4 h at 4 °C. After fixation, we then washed the solution three times with water, allowing 10 min for each wash on a shaker table. Afterwards, a 4% aqueous osmium tetroxide solution was diluted to 1% by mixing with 3 ml of PBS. This 1% osmium tetroxide solution was used for post-fixation in a dark environment within a hood for 100 min. Finally, the solution underwent washing procedures following the same process as described earlier. Both normal oblate-shaped RBCs and abnormal spherical-shaped RBCs generated from normal cells *via* NaCl treatment were fixed separately to preserve their respective morphologies. Following fixation, the two RBC populations were collected into separate tubes for subsequent analysis. To enable clear differentiation between the cell shapes during fluorescence-based quantification, a shape-specific membrane staining protocol was implemented.[55] Normal oblate-shaped RBCs were labeled with green fluorescent FITC-dextran (70 kDa, 100 μg mL^{-1}), while abnormal spherical-shaped RBCs were stained with red fluorescence with the help of a LIVE/DEAD BacLight Bacterial Viability Kit (DMSO 30 μL mL^{-1}) and 2 μL mL^{-1} each of the two Invitrogen Live/Dead stains (orange and purple). The kit uses a dye called propidium iodide, which can only enter cells with damaged membranes, causing them to fluoresce red. Since abnormally shaped or damaged RBCs may have compromised membranes, they would also be stained red by this dye.[56] The staining was performed in the dark for 30 min to ensure consistent membrane labeling and minimize photobleaching. This dual-color staining approach allows reliable identification and quantitative comparison of RBCs based on their shape during post-collection fluorescence analysis.

All procedures performed in this study were conducted in accordance with the Bioethics and Safety Act of the Republic of Korea and the ethical principles outlined in the Declaration of Helsinki. The study also follows the guidelines of Chonnam National University and complies with Korean Good Clinical Practice (KGCP) and International Council for Harmonisation (ICH) standards. This study was reviewed and approved by the Institutional Review Board (IRB) of Chonnam National University (IRB No. 1040198-230705-BR-085-03). The requirement for informed consent was waived by the IRB due to the exclusive use of fully anonymized human-derived samples, with no identifiable personal information involved.

Author contributions

M. S. K.: writing – original draft (lead); investigation (lead). M. A.: investigation (supporting). Y. B. B.: investigation (supporting). S. J. L.: conceptualization (supporting); writing – review & editing (supporting). J. P.: conceptualization (lead); funding acquisition (lead); writing – review & editing (lead).

Conflicts of interest

There are no conflicts to declare.

Data availability

All data reported in this work are available from the corresponding author upon reasonable request. The supplementary information (SI) associated with this article includes: derivation of the acoustic radiation torque and force along with radiation force function (Y_p); numerical investigation of asymmetric wave scattering from oblate spheroids with varying orientation and aspect ratio; acoustic radiation force factor (F_F) graphs with varying acoustic wave frequency (f) and the PS particle and RBCs diameter (d_p) (Fig. S1); Fig. S2 (supporting experimental results for Fig. 6); Fig. S3 shows S_{11} measurement data of both IDTs by a vector network analyzer; Fig. S4 indicates roles of ART and ARF in particle orientation and particle vertical migration. Movie S1 (illustrating movement of spherical and oblate particle in an acoustic field).

Supplementary information is available. See DOI: https://doi.org/10.1039/d6lc00140h.

Acknowledgements

J. P. acknowledges the National Research Foundation of Korea (NRF) grants funded by the Korea government (MSIT) (No. RS-2023-00210891 and RS-2020-NR049568). The microfluidic devices were fabricated by using a mask aligner (MDA-400S, MIDAS) at the Energy Convergence Core Facility at Chonnam National University. S. J. L. acknowledges the support by the National Research Foundation of Korea (NRF-2021R1F1A1063116).

References

1 M. Luciano, M. Versaevel, E. Vercruysse, A. Procès, Y. Kalukula and A. Remson, *et al.*, Appreciating the role of cell shape changes in the mechanobiology of epithelial tissues, *Biophys. Rev.*, 2022, **3**(1), 011305.
2 J. N. Thon and J. E. Italiano, Platelets: production, morphology and ultrastructure, *Handb. Exp. Pharmacol.*, 2012(210), 3–22.
3 B. K. Byrd, V. Krishnaswamy, J. Gui, T. Rooney, R. Zuurbier and K. Rosenkranz, *et al.*, The shape of breast cancer, *Breast Cancer Res. Treat.*, 2020, **183**(2), 403–410.
4 R. Kano, Emergence of Fungal-Like Organisms: Prototheca, *Mycopathologia.*, 2020, **185**(5), 747–754.
5 R. Braun-Nesje, K. Bertheussen, G. Kaplan and R. Seljelid, Salmonid macrophages: Separation, in vitro culture and characterization, *J. Fish Dis.*, 2006, **4**, 141–151.
6 D. Ribatti, R. Tamma and T. Annese, Epithelial-Mesenchymal Transition in Cancer: A Historical Overview, *Transl. Oncol.*, 2020, **13**(6), 100773.
7 M. Franchi, Z. Piperigkou, K.-A. Karamanos, L. Franchi and V. Masola, Extracellular Matrix-Mediated Breast Cancer Cells Morphological Alterations, Invasiveness, and Microvesicles/Exosomes Release, *Cell*, 2020, **9**(9), 2031.
8 K. S. Peter, Red blood cells, *Int. J. Biochem. Cell Biol.*, 2002, **34**(12), 1513–1518.
9 J. Ford, Red blood cell morphology, *Int. J. Lab. Hematol.*, 2013, **35**(3), 351–357.
10 L. Tyrrell, G. Rose, A. Shukri and S. B. Kahwash, Morphologic changes in red blood cells: An illustrated review of clinically important light microscopic findings, *Malays. J. Pathol.*, 2021, **43**(2), 219–239.
11 A. K. Dasanna, S. Hillringhaus, G. Gompper and D. A. Fedosov, Effect of malaria parasite shape on its alignment at erythrocyte membrane, *Elife.*, 2021, **10**, 68818.
12 S. Perrotta, P. G. Gallagher and N. Mohandas, Hereditary spherocytosis, *Lancet*, 2008, **372**(9647), 1411–1426.
13 D. C. Rees, T. N. Williams and M. T. Gladwin, Sickle-cell disease, *Lancet*, 2010, **376**(9757), 2018–2031.
14 C. Robier, D. Klescher, G. Reicht, O. Amouzadeh-Ghadikolai, F. Quehenberger and M. Neubauer, Dacryocytes are a common morphologic feature of autoimmune and microangiopathic haemolytic anaemia, *Clin. Chem. Lab. Med.*, 2015, **53**(7), 1073–1076.
15 M. Diez-Silva, M. Dao, J. Han, C.-T. Lim and S. Suresh, Shape and Biomechanical Characteristics of Human Red Blood Cells in Health and Disease, *MRS Bull.*, 2010, **35**(5), 382–388.
16 M. C. F. van Teeseling, M. A. de Pedro and F. Cava, Determinants of Bacterial Morphology: From Fundamentals to Possibilities for Antimicrobial Targeting, *Front. Microbiol.*, 2017, **8**, 1264.
17 B. Behdani, S. Monjezi, M. J. Carey, C. G. Weldon, J. Zhang and C. Wang, *et al.*, Shape-based separation of micro–/nanoparticles in liquid phases, *Biomicrofluidics*, 2018, **12**(5), 051503.

18 Q. Wei, Y. Xiong, Y. Ma, D. Liu, Y. Lu and S. Zhang, *et al.*, High-throughput single-cell assay for precise measurement of the intrinsic mechanical properties and shape characteristics of red blood cells, *Lab Chip*, 2024, **24**(2), 305–316.
19 M. S. Khan, R. H. Julio, M. Ali, S. Sachs, C. Cierpka and J. König, *et al.*, Microfluidic shape-based separation for cells and particles: recent progress and future perspective, *Lab Chip*, 2026, **26**, 1025–1052.
20 S. C. Hur, S.-E. Choi, S. Kwon and D. D. Carlo, Inertial focusing of non-spherical microparticles, *Appl. Phys. Lett.*, 2011, **99**(4), 044101.
21 M. Li, H. E. Muñoz, K. Goda and D. Di Carlo, Shape-based separation of microalga Euglena gracilis using inertial microfluidics, *Sci. Rep.*, 2017, **7**(1), 10802.
22 M. Jiang, K. Budzan and G. Drazer, Fractionation by shape in deterministic lateral displacement microfluidic devices, *Microfluid. Nanofluid.*, 2015, **19**(2), 427–434.
23 S. H. Holm, J. P. Beech, M. P. Barrett and J. O. Tegenfeldt, Separation of parasites from human blood using deterministic lateral displacement, *Lab Chip*, 2011, **11**(7), 1326–1332.
24 M. Matsuda, M. Yamada and M. Seki, Blood cell classification utilizing hydrodynamic filtration, *Electron. Commun. Jpn.*, 2011, **94**(1), 1–6.
25 J. Dual, P. Hahn, I. Leibacher, D. Möller, T. Schwarz and J. Wang, Acoustofluidics 19: Ultrasonic microrobotics in cavities: devices and numerical simulation, *Lab Chip*, 2012, **12**(20), 4010–4021.
26 P. Hahn, I. Leibacher, T. Baasch and J. Dual, Numerical simulation of acoustofluidic manipulation by radiation forces and acoustic streaming for complex particles, *Lab Chip*, 2015, **15**(22), 4302–4313.
27 P. Hahn, A. Lamprecht and J. Dual, Numerical simulation of micro-particle rotation by the acoustic viscous torque, *Lab Chip*, 2016, **16**(23), 4581–4594.
28 S. Sachs, H. Schmidt, C. Cierpka and J. König, On the behavior of prolate spheroids in a standing surface acoustic wave field, *Microfluid. Nanofluid.*, 2023, **27**(12), 81.
29 Y. Chen, X. Ding, S.-C. Steven Lin, S. Yang, P.-H. Huang and N. Nama, *et al.*, Tunable Nanowire Patterning Using Standing Surface Acoustic Waves, *ACS Nano*, 2013, **7**(4), 3306–3314.
30 M. S. Khan, M. Ali, S. H. Lee, K. Y. Jang, S. J. Lee and J. Park, Acoustofluidic separation of prolate and spherical micro-objects, *Microsyst. Nanoeng.*, 2024, **10**(1), 6.
31 M. Ali, M. S. Khan, J. Park, C. Zhang and J. Park, Tilted-angle acoustofluidics for particle and cell manipulation: Fundamentals, strategies, and outlook, *Biomed. Instrum.*, 2026, **2**(1), 100039.
32 J. Koh, J. Kim, J. H. Shin and W. Lee, Fabrication and integration of microprism mirrors for high-speed three-dimensional measurement in inertial microfluidic system, *Appl. Phys. Lett.*, 2014, **105**(11), 114103.
33 A. Pasha, S. Khasim, A. A. A. Darwish, T. A. Hamdalla, S. A. Al-Ghamdi and S. Alfadhli, Flexible, stretchable and electrically conductive PDMS decorated with polypyrrole/manganese-iron oxide nanocomposite as a multifunctional material for high performance EMI shielding applications, *Synth. Met.*, 2022, **283**, 116984.
34 J. Park, B. Cha, F. G. Almus, M. A. Sahin, H. Kang and Y. Kang, *et al.*, Acoustic Waves Coupling with Polydimethylsiloxane in Reconfigurable Acoustofluidic Platform, *Adv. Sci.*, 2024, **11**(47), 2407293.
35 M. S. Khan, W. Kim and J. Park, Reconfigurable acoustofluidic platform with vacuum pressure-assisted reversible bonding, *Sens. Actuators, B*, 2026, **458**, 139847.
36 D. J. Collins, T. Alan and A. Neild, Particle separation using virtual deterministic lateral displacement (vDLD), *Lab Chip*, 2014, **14**(9), 1595–1603.
37 M. S. Khan, M. A. Sahin, G. Destgeer and J. Park, Residue-free acoustofluidic manipulation of microparticles via removal of microchannel anechoic corner, *Ultrason. Sonochem.*, 2022, **89**, 106161.
38 M. A. S. Pessôa and A. A. R. Neves, Acoustic scattering and forces on an arbitrarily sized fluid sphere by a general acoustic field, *J. Sound Vib.*, 2020, **479**, 115373.
39 J. P. Leão-Neto, J. H. Lopes and G. T. Silva, Acoustic radiation torque exerted on a subwavelength spheroidal particle by a traveling and standing plane wave, *J. Acoust. Soc. Am.*, 2020, **147**(4), 2177.
40 F. G. Mitri, Acoustic backscattering and radiation force on a rigid elliptical cylinder in plane progressive waves, *Ultrasonics*, 2016, **66**, 27–33.
41 Z. Fan, D. Mei, K. Yang and Z. Chen, Acoustic radiation torque on an irregularly shaped scatterer in an arbitrary sound field, *J. Acoust. Soc. Am.*, 2008, **124**(5), 2727–2732.
42 F. G. Mitri, Radiation forces and torque on a rigid elliptical cylinder in acoustical plane progressive and (quasi)standing waves with arbitrary incidence, *Phys. Fluids*, 2016, **28**(7), 077104.
43 F. B. Wijaya and K. M. Lim, Numerical calculation of acoustic radiation force and torque on non-spherical particles in Bessel beams, *Proc. Meetings Acoust.*, 2016, **26**(1), 045002.
44 T. Tohme, P. Magaud and L. Baldas, Transport of Non-Spherical Particles in Square Microchannel Flows: A Review, *Micromachines*, 2021, **12**(3), 277.
45 S. Yang, J. Y. Kim, S. J. Lee, S. S. Lee and J. M. Kim, Sheathless elasto-inertial particle focusing and continuous separation in a straight rectangular microchannel, *Lab Chip*, 2011, **11**(2), 266–273.
46 J. Kim, J. Y. Kim, Y. Kim, S. J. Lee and J. M. Kim, Shape Measurement of Ellipsoidal Particles in a Cross-Slot Microchannel Utilizing Viscoelastic Particle Focusing, *Anal. Chem.*, 2017, **89**(17), 8662–8666.
47 S. J. Ahn, K. H. Ahn and S. J. Lee, Film squeezing process for generating oblate spheroidal particles with high yield and uniform sizes, *Colloid Polym. Sci.*, 2016, **294**(5), 859–867.

48 S. Z. Hoque, K. Bhattacharyya and A. K. Sen, Dynamical motion of an oblate shaped particle exposed to an acoustic standing wave in a microchannel, *Phys. Rev. Fluids*, 2022, **7**(11), 114204.
49 D. J. Collins, T. Alan and A. Neild, The particle valve: On-demand particle trapping, filtering, and release from a microfabricated polydimethylsiloxane membrane using surface acoustic waves, *Appl. Phys. Lett.*, 2014, **105**(3), 033509.
50 H. Ahmed, G. Destgeer, J. Park, J. H. Jung and H. J. Sung, Vertical Hydrodynamic Focusing and Continuous Acoustofluidic Separation of Particles via Upward Migration, *Adv. Sci.*, 2018, **5**(2), 1700285.
51 W. H. Reinhart, N. Z. Piety, J. S. Goede and S. S. Shevkoplyas, Effect of osmolality on erythrocyte rheology and perfusion of an artificial microvascular network, *Microvasc. Res.*, 2015, **98**, 102–107.
52 M. Sesen, T. Alan and A. Neild, Microfluidic on-demand droplet merging using surface acoustic waves, *Lab Chip*, 2014, **14**(17), 3325–3333.
53 L. D. Piegols, T. Dwyer, S. C. Glotzer and O. Eniola-Adefeso, Shape-Dependent Structural Order of Red Blood Cells, *Langmuir*, 2025, **41**(3), 1876–1888.
54 O. M. Ikumapayi, E. T. Akinlabi, A. O. M. Adeoye and S. O. Fatoba, Microfabrication and nanotechnology in manufacturing system – An overview, *Mater. Today: Proc.*, 2021, **44**, 1154–1162.
55 X. Dong, Y. Niu, Y. Ding, Y. Wang, J. Zhao and W. Leng, *et al.*, Formulation and Drug Loading Features of Nano-Erythrocytes, *Nanoscale Res. Lett.*, 2017, **12**(1), 202.
56 L. Boulos, M. Prévost, B. Barbeau, J. Coallier and R. Desjardins, LIVE/DEAD BacLight: application of a new rapid staining method for direct enumeration of viable and total bacteria in drinking water, *J. Microbiol. Methods*, 1999, **37**(1), 77–86.